

Cite this: *Energy Environ. Sci.*,
2020, 13, 4930

All ceramic cathode composite design and manufacturing towards low interfacial resistance for garnet-based solid-state lithium batteries†

Kun Joong Kim ^a and Jennifer L. M. Rupp ^{*ab}

The critical factors that determine the performance and lifetime of solid-state batteries (SSBs) are driven by the electrode–electrolyte interfaces. The main challenge in fabricating all-oxide cathode composites for garnet-based SSBs has been lowering the thermal processing window in which both good contact and low interfacial resistance can be achieved. Here, we report an alternative ceramic processing strategy that enables the fabrication of all-oxide composite cathodes at an unusually low processing temperature without the use of extra sintering additives or a fluid electrolyte (polymer-gel or liquid electrolyte). We present specific examples of the most common LiFePO_4 and LiCoO_2 cathodes with a Li-garnet ($\text{Li}_7\text{La}_3\text{Zr}_2\text{O}_{12}$, LLZO) solid-electrolyte. We demonstrate an infiltration step to directly synthesize the LiCoO_2 cathode from metal salts in a porous LLZO scaffold, resulting in the formation of a composite cathode such as LiCoO_2 –LLZO on top of a dense LLZO solid electrolyte at a low processing temperature of 700 °C. A promising discharge capacity of 118 mA h g^{-1} (3–4.05 V) with a low interfacial resistance of 62 $\Omega\text{ cm}^2$ is realized for LiCoO_2 with a lithium anode, whereas critical phase instabilities for LiFePO_4 are uncovered. Our findings encourage a move away from synthesis techniques that employ particle mixing and sintering to fabricate composites. We provide a blueprint for circumventing adverse interphase reactions according to chemistry and ceramic thermal processing budgets in the preparation of these ceramic interfaces as well as for increasing the number of reaction sites for high-performing composite cathodes for Li-garnet SSBs. In addition, the ceramic methods presented are scalable and mass manufacturable for the large-scale production of such composite cathodes for future industry.

Received 29th June 2020,
Accepted 5th October 2020

DOI: 10.1039/d0ee02062a

rsc.li/ees

Broader context

Solid-state batteries based on inorganic solid electrolytes offer safer alternatives to classical lithium-ion batteries due to their non-flammable nature and give prospects of both high energy and power densities. Among them, sulfide- and oxide-based solid-state battery architectures have attracted continuing attention due to their high ionic conductivity and stability with Li metal. Despite the promise of superior chemical and electrochemical stability of oxide-type batteries during cell operation, fabrication difficulties in achieving mechanically rigid and chemically pure interfaces between the cathode and oxide electrolyte have been serious challenges. Oxide batteries typically reveal high interfacial impedance and readily fail to reach the theoretical capacity of the active cathode material. Here, we introduce a low-temperature fabrication route for an oxide-type cathode composite that can enhance the specific capacity and interfacial resistance by avoiding detrimental interfacial reactions and maximizing active reaction sites. We hope to provide the reader with an overview of existing cathode preparation options and new insights that constitute a step forward in unravelling the complex interplay between ceramic processing routes and performance during oxide battery fabrication.

Introduction

Solid-state batteries (SSBs) based on solid electrolytes and Li metal anodes are considered safer and higher energy alternatives to conventional batteries operating with combustible liquid electrolytes.¹ After sustained research efforts, solid electrolytes now possess conductivities that are competitive with those of liquid electrolytes.² For example, oxide-type Li garnets such as $\text{Li}_7\text{La}_3\text{Zr}_2\text{O}_{12}$ (LLZO) have exhibited conductivities

^a Electrochemical Materials Laboratory, Department of Materials Science and Engineering, Massachusetts Institute of Technology, Cambridge, Massachusetts 02139, USA. E-mail: jrupp@mit.edu

^b Electrochemical Materials Laboratory, Department of Electrical Engineering and Computer Science, Massachusetts Institute of Technology, Cambridge, Massachusetts 02139, USA

† Electronic supplementary information (ESI) available. See DOI: 10.1039/d0ee02062a



greater than 1 mS cm^{-1} and can be processed as ceramics in the form of pellets, tapes, and films over a wide temperature range with a wide variety of thicknesses.^{3,4} Among SSB electrolyte materials, LLZO^{5,6} offers a relatively wide electrochemical stability window (along with LIPON⁷⁻⁹) as well as compatibility with the high-capacity lithium anode.¹⁰ Promising critical current densities as high as 10 mA cm^{-2} have been demonstrated in lithium symmetrical cells based on tri-layer LLZO electrolytes,¹¹ resulting in their ranking among promising future SSB architectures. From a processing perspective, there have been numerous attempts to achieve good contact between the lithium anode and LLZO electrolyte. Thanks to these efforts, novel strategies to achieve a LLZO–Li interfacial resistance as low as several $\Omega \text{ cm}^2$ are available.^{3,6,12-16} However, interfacial design and fabrication strategies that result in low interfacial resistance across the LLZO–cathode interface and within the cathode composite require further attention.^{17,18} For instance, the interfacial resistance for Li-garnet SSB cells has been reported to be readily over thousands of $\Omega \text{ cm}^2$. The state-of-the-art cell consisting of LiCoO_2 , $\text{Li}_{2.3}\text{C}_{0.7}\text{B}_{0.3}\text{O}_3$, and LLZO as the cathode composite, LLZO as the electrolyte, and a Li metal anode exhibits a total interfacial resistance of approximately $270 \Omega \text{ cm}^2$ at 100°C , which is predominantly attributed to the resistance of the LLZO–cathode interface.¹⁹ The origin of the high interfacial resistance can be generally explained by either the formation of insulating phases at the interfaces at the cell fabrication temperature (700°C) or weak mechanical bonding between the cathode and LLZO electrolyte if the co-sintering temperature was too low. Nonetheless, recent holistic analysis on the performance of state-of-the-art SSBs has suggested that a high-specific-energy cell requires less than approximately $40 \Omega \text{ cm}^2$ internal resistance to allow targeted cycling at 1C with more than 90% energy efficiency.^{20,21} To commercialize these generally established active materials of Li cobaltite, Li phosphate, and Li titanate for future Li-garnet SSB products, appropriate ceramic synthesis routes to prepare suitable LLZO–cathode composites need to be investigated.

Recent progress on such cathode composite processing in Li-garnet SSBs has led to the identification of three major strategies for their assembly that define the thermal processing window, tested active materials and loading (wt%) of the active cathode storage material: (i) hybrid cathodes, (ii) all-oxide cathodes with additives, and (iii) all-oxide cathodes without additives, as illustrated in Fig. 1a.

Hybrid cathodes composed of liquid- or polymer-based catholytes (the part of the electrolyte on the cathode side of an electrochemical cell) mixed with active materials and carbon (Fig. 1a) are in principle a copy-cat cathode design of the cathodes used in traditional lithium-ion batteries, with the porous polymer separator simply replaced by a LLZO electrolyte. Cells with hybrid cathodes based on LiCoO_2 ,²² LiFePO_4 ,²³⁻²⁵ $\text{Li}(\text{Ni},\text{Co},\text{Mn})\text{O}_2$,^{26,27} $\text{Li}_2\text{FeMn}_3\text{O}_8$,¹² and sulfur^{11,28} have been reported, and various forms of catholytes consisting of Li salts in an organic solvent or polymer matrix, namely liquid electrolytes,¹² polymer-gels,^{23,24} ionic liquids,^{22,26} and plastic crystals,²⁷ have been tested. The liquid catholyte penetrates the

as-cast porous cathode sheet, Fig. 1a(i), allowing sufficiently large contact area on its surface and forming a percolating network for sufficient ion transport. Typically, the hybrid cathode processing includes casting of a slurry prepared by mixing the active materials (crystallized oxide particles), a binder, and carbon as the conducting agent in a solvent and drying at approximately $80\text{--}150^\circ\text{C}$, followed by infiltration of the catholyte. Such easy processing at low temperature (no sintering required) makes the hybrid cathode design attractive with a high cathode loading of $>90 \text{ wt}\%$. The reduced amount of flammable or less thermodynamically stable catholyte in hybrid-cathode Li-garnet SSBs compared with that in a typical liquid battery system may be advantageous for safety.^{2,3} For these reasons, such a hybrid SSB design is gaining momentum; however, the underlying interfacial reaction requires further investigation^{29,30} and practical demonstrations targeting cycle numbers >500 and C-rates $>1\text{C}$ are needed.³

In contrast, an all-oxide cathode uses purely inorganic ceramic materials for the electrolyte and cathode constituents forming a composite cathode, as shown in Fig. 1a(ii) and (iii). The main merit of all-oxide cathodes over hybrid cathodes is overall battery safety against thermal runaway by completely avoiding flammable liquid catholytes or organic electrolytes.³¹ However, it is difficult to realize strong bonding within the composite network with low interfacial resistance. Furthermore, high active material loading is difficult to achieve as shown by recent reports with only $50\text{--}58 \text{ wt}\%$,^{19,32-37} which makes the realization of high energy density difficult.

With or without additives, all-oxide cathode composite fabrication involves the preparation of a slurry solution (composed of the solid electrolyte and electrode particles, binder, and solvent), followed by screen printing of the composite slurry onto the LLZO electrolyte and sintering (Fig. 1b). With increasing temperature, the organic binder is first burned out, and three different types of solid–solid contacts are made (*i.e.*, $\text{LiCoO}_2\text{--LiCoO}_2$, LLZO--LiCoO_2 , and LLZO--LLZO), followed by grain growth and neck growth among the constituent phases. For instance, a cathode composite with Ta-doped LLZO and LiCoO_2 can be made with mechanically strong bonding *via* solid-state diffusion at 1050°C ,³⁷ thereby meeting one of the requirements for low interfacial resistance. However, possible side reactions can occur during such high-temperature processes and may increase the interfacial resistance ($1138 \Omega \text{ cm}^2$), reducing the specific capacity below the theoretical one.³⁷ Furthermore, this approach would be exclusive to these phases and would not apply for many other oxide cathodes because of their higher reactivity with LLZO.³⁸ For instance, a pellet-based compatibility study³⁹ shows that Li-insulating interphases begin to form at above 600°C in LLZO cathode composites with high-voltage active materials of $\text{Li}_2\text{NiMn}_3\text{O}_8$, $\text{Li}_2\text{FeMn}_3\text{O}_8$, and LiCoMnO_4 . In addition, the chemical reactivity and decomposition of composite cathode pellets were confirmed for LLZO--LiCoO_2 and $\text{LLZO--LiNi}_{0.33}\text{Co}_{0.33}\text{Mn}_{0.33}\text{O}_2$ at 700°C and even at 500°C for $\text{LLZO--LiMn}_2\text{O}_4$ and LLZO--LiFePO_4 .^{40,41}

Sintering additives can be used to facilitate the particle interconnection and densification of the cathode and electrolyte



lithium-ion batteries⁵⁴ that has never been investigated as a composite cathode for all-oxide SSBs with Li garnets.

In an initial attempt, prior to the fabrication of a full cell with a LiFePO_4 -based composite cathode (LiFePO_4 -LLZO-carbon), we first explored the phase compatibility between LiFePO_4 and LLZO using composite pellets (50:50 wt%) fired over a wide temperature range from 250 °C to 1000 °C. XRD patterns were obtained and the pellet color was monitored using light microscopy for each firing temperature to analyze the phase constituents (Fig. 3a). With increasing firing temperature, we observed changes in the apparent XRD phases and sample color of the LiFePO_4 -LLZO composites. For the composite pellet with no heat treatment, two separated XRD signatures consistent with the LLZO and LiFePO_4 phases were observed.⁴¹ At 250 °C, little changed in the X-ray patterns and the pellet color. After firing to 300 °C, we detected minor XRD peaks at 23.2° and 36.1°, corresponding to small quantities of the $\text{Li}_3\text{Fe}_2(\text{PO}_4)_3$ phase. We observed more pronounced peaks

indicative of the $\text{Li}_3\text{Fe}_2(\text{PO}_4)_3$ and Fe_2O_3 phases and a color change at 350–400 °C. Firing between 600 °C and 1000 °C prompted the decomposition of $\text{Li}_3\text{Fe}_2(\text{PO}_4)_3$ and LLZO, leaving detectable quantities of LaPO_4 , Li_3PO_4 , $\text{La}_2\text{Zr}_2\text{O}_7$, and Fe_2O_3 in the XRD pattern. According to this phase compatibility analysis, we concluded that the desired LiFePO_4 phase only allowed for a very narrow processing window of approximately up to 300 °C for co-sintering with LLZO without sacrificing interfacial reactions. The reaction temperature is an even lower than that reported in recent compatibility study, as they performed sintering of a LiFePO_4 -LLZO pellet in a reducing atmosphere.⁴¹

We assembled composite cathodes based on LiFePO_4 -LLZO-carbon (with 55:25:20 wt%) in the LLZO scaffold-pellet assembly and integrated a Li metal anode to investigate the electrochemistry and interfacial resistance by varying the cathode firing temperature from 250 °C to 400 °C (Fig. 3b). The cathode composite thickness was approximately 42 μm (Fig. S2, ESI[†]). The cathode composites fired at 300 °C exhibited the

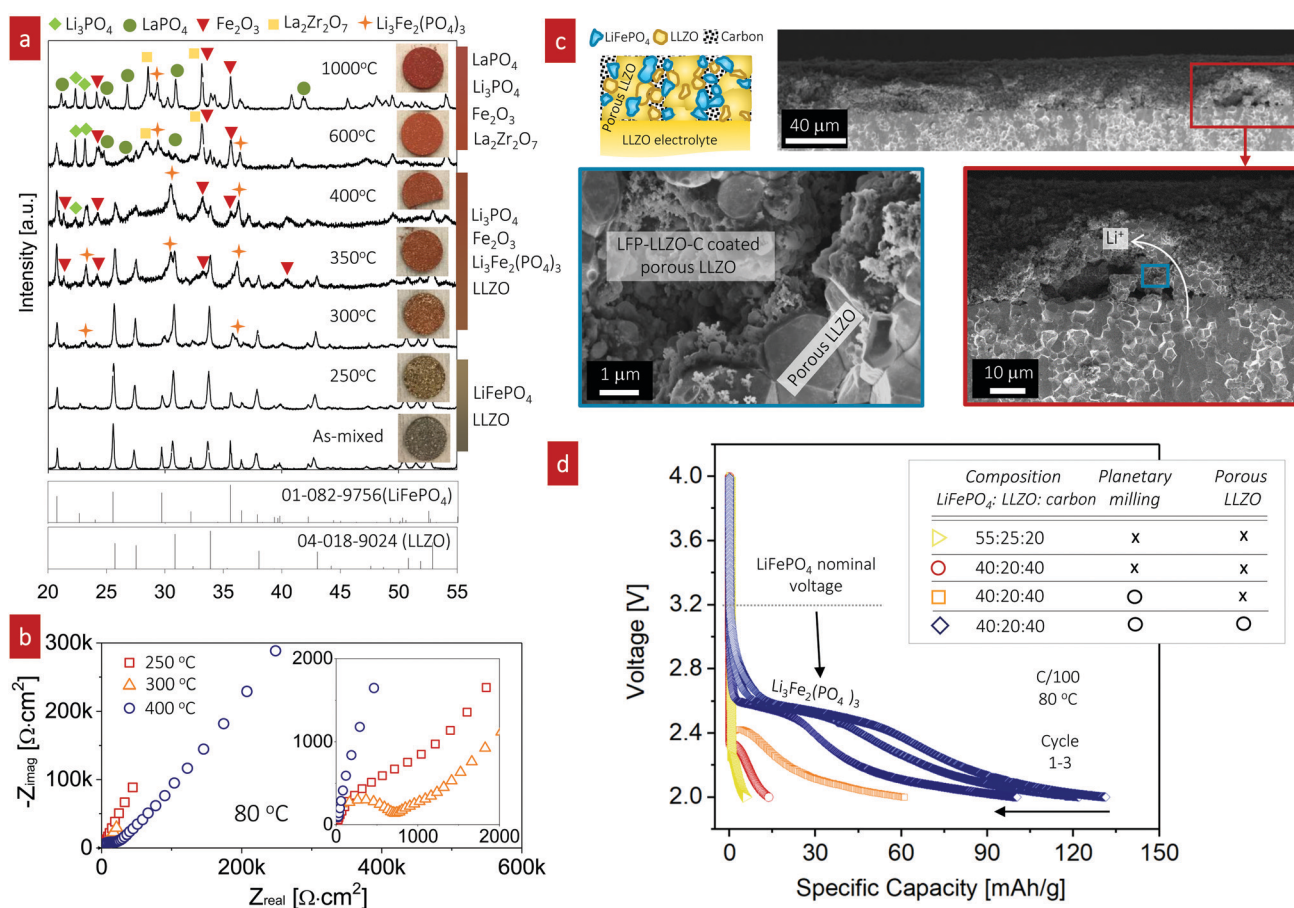


Fig. 3 Characterization and fabrication of LiFePO_4 -based cathode composite cathodes for all-oxide Li-garnet SSBs. (a) Chemical compatibility study of the LiFePO_4 and LLZO interface with the cathode firing temperature ranging from room temperature to 1000 °C. The inset presents images of the as-fired composite model pellet. (b) Impedance spectra of the full cell (LiFePO_4 -LLZO-carbon|LLZO|Li) with the cathode firing temperature ranging from 250 °C to 400 °C. The cathode fired at 300 °C exhibited the lowest total cell resistance among the tested cells. (c) Schematic illustration and cross-sectional SEM images of the interface-engineered cathode composite. A schematic image and associated cross-sectional SEM images captured at low, moderate (red box), and high magnification (blue box) are shown, confirming the good contact between the cathode compounds and porous LLZO scaffold layer (blue box). (d) Discharge capacities of full cells with the cathode composite as a function of composition, planetary milling, and interface engineering.



of crystalline cathode particles.^{37,61,62} In contrast, in our approach, we use cathode precursor solution infiltration into a porous LLZO scaffold followed by crystallization to the oxide cathode directly from the metal salt constituents. Using such altered pathways in ceramic processing and shaping the cathode composites has the significant advantage of strongly reducing the temperature at which good bonding is achieved without adverse chemical reactions. Importantly, the cathode is directly crystallized on the large surface area of porous LLZO; thus, the active reaction area can be controlled dependent on the microstructure (porosity and thickness) of the porous LLZO. As demonstrated in the previous section with our proposed infiltration using the LLZO scaffold method for the composite cathode on LiFePO₄-LLZO, we now turn to the LiCoO₂-LLZO system as a tandem material for further exploration and adaption of the technique.

In line with this ceramic process design for the composite, we selected a firing temperature of 700 °C (Fig. 4a) as it is the minimum temperature that results in crystallization of LiCoO₂ particles from the Li-Co-O precursor solution without any sign of an amorphous phase (Fig. S5, ESI[†]). Cross-sectional SEM analysis revealed a well-connected network composed of LLZO grains with a diameter of 2.3 ± 0.1 μm (Fig. 4b) and LiCoO₂ grains with a diameter of 0.29 ± 0.020 μm with fairly good coverage on the surface of porous LLZO (Fig. 4c). EDS mapping of the interface at LiCoO₂-LLZO revealed separated Co- and La-rich regions across the microstructure of the composite cathode (Fig. 4d and Fig. S6, ESI[†]). To explore the local phase stability after processing of the cathode composites, we performed Raman spectroscopy analysis across the interface region of the dense LLZO pellet and toward the cathode composite (Fig. 4e). The Raman spectra for LLZO contained

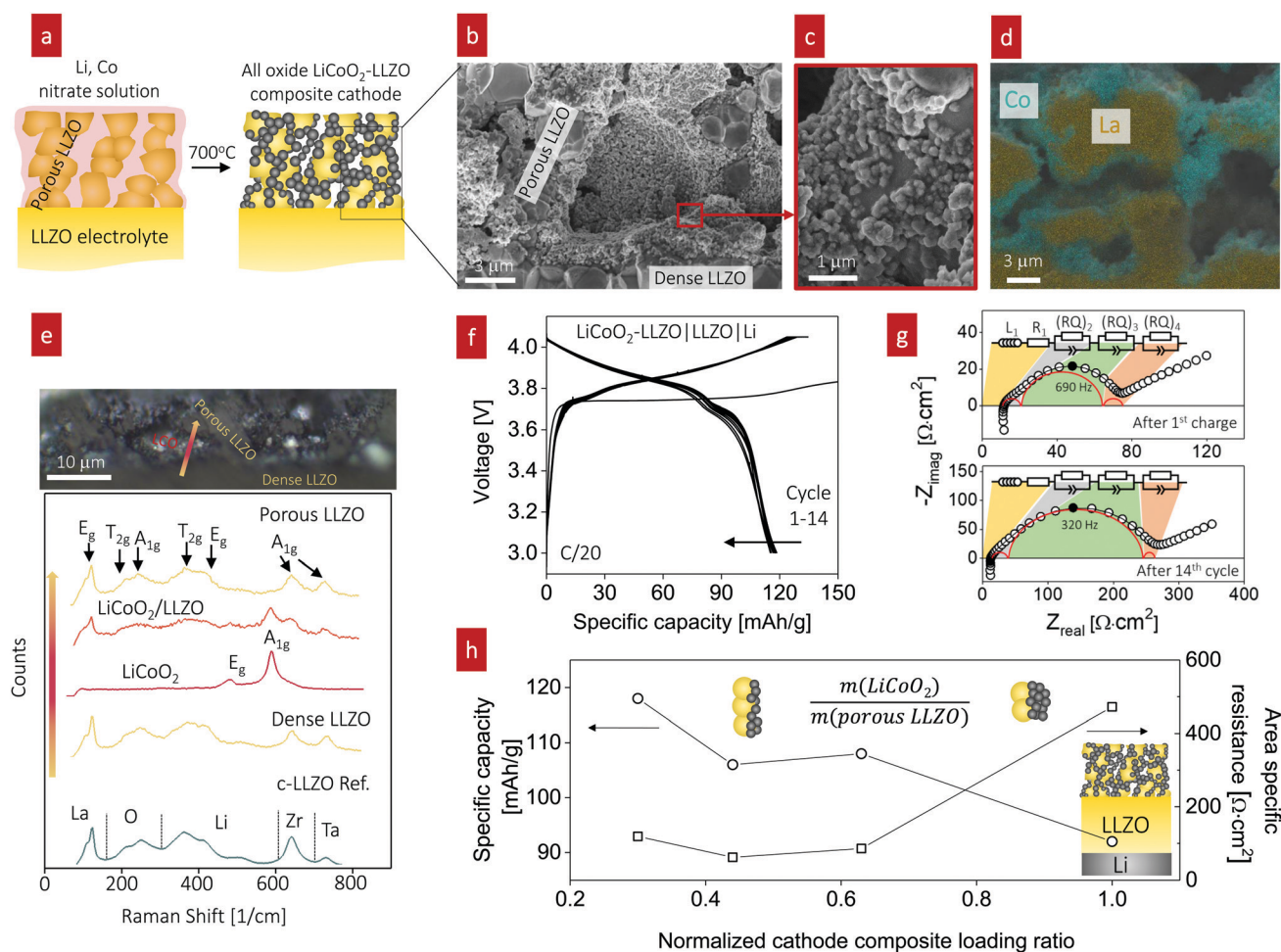


Fig. 4 Characterization and fabrication of LiCoO₂-based composite cathodes for all-oxide Li-garnet SSBs. (a) Schematic illustration of the composite cathode prepared by direct infiltration of Li and Co metal salts into a pre-made porous LLZO scaffold and subsequent firing at 700 °C, resulting in the formation of the composite on top of a dense LLZO solid electrolyte. (b–d) SEM images and EDS mapping of the LiCoO₂-LLZO cathode composite. (e) Optical image and corresponding Raman spectra with different points at the interface through the electrolyte pellet, LiCoO₂, and porous LLZO after firing at 700 °C. (f) Cycling performance of the full cell (LiCoO₂-LLZO|LLZO|Li) at 0.05C and 80 °C. (g) Impedance spectra of the full cell at open-circuit potential after charging. (h) Change in specific capacity (mA h g⁻¹) and area specific resistance (ASR, Ω cm²) with regard to the normalized composite loading ratio $\frac{m(\text{LiCoO}_2)}{m(\text{LLZO})}$. The inset presents a schematic illustration of the cathode microstructure. With decreased loading ratio, improved cathode utilization and ASR are achieved due to the increased surface area of LLZO and shorter Li-ion diffusion distance.



LCO/LLZO interfaces, it is important to employ high-resolution or *in situ* characterization techniques to elucidate the changes in the microstructure and chemistry at the interfaces^{75,76} together with *in situ* impedance studies. In addition to understanding the degradation mechanism, further minimization of the interfacial reaction down to the target value of $\sim 40 \Omega \text{ cm}^2$ is needed for enhanced performance.²⁰ The low self-discharge rate during the rest (Fig. S13, ESI[†]) suggests limited electronic leakage (1.14%) in the full cell, potentially indicating that cobalt contamination in the LLZO electrolyte during cell fabrication can be excluded. However, a slight increase of the self-discharge up to 1.24% with cycling was observed.

In the next step, we highlight one of the measures for understanding the relationship between cathode microstructure and performance (Fig. 4h). Assuming that the LiCoO₂ cathode covers the entire surface area of the porous LLZO, the number of active reaction sites can be controlled either by adjusting the solid loading (or porosity) of the porous LLZO or the amount of LiCoO₂ loading, which directly affects the cathode performance and interfacial resistance. To test this scenario, we varied the solid loading of the porous LLZO (6.41–18.6 mg cm⁻²) under a rather fixed amount of LiCoO₂ (0.73–1.4 mg cm⁻²) and evaluated the effect on the performance. Microscopically, this translates to changes in the arrangement and coverage of LiCoO₂ particles on the porous LLZO backbone. Notably, we observed that both the specific capacity and total area specific resistance (ASR) were largely affected by the composite loading ratio, defined as $\frac{m(\text{LiCoO}_2)}{m(\text{LLZO})}$. For simplification, the change was normalized from 0 to 1. When this normalized composite ratio decreased from 1 to 0.3, the specific capacities increased from 91 to 118 mA h g⁻¹ with decreasing total ASR from 472 to 114 $\Omega \text{ cm}^2$. A decreased loading ratio implies that there is more empty area for LiCoO₂ to directly contact with the porous LLZO scaffold instead of a LiCoO₂–LiCoO₂ contact as schematically illustrated as an inset. An increase in the LLZO loading also leads to lower current densities in the cathode composite (at the porous LLZO and at the LCO/LLZO interfaces) owing to the increased ionic surface area or LCO/LLZO interfacial length. The number of reaction sites at electrode/electrolyte interfaces is of vital importance to achieve reduced cell polarization and improved capacity. In this work, the cathode microstructure with an optimized solid loading of $\frac{m(\text{LiCoO}_2)}{m(\text{LLZO})} \leq 0.3$ is expected to show a shorter Li-ion diffusion distance with lowered current densities in LLZO during the electrochemical reaction. Therefore, improved cathode utilization and interfacial resistance are achieved. It is, however, important to note that optimization can also be achieved by manipulating another descriptor such as the porosity under the consideration of effective reaction sites. We successfully demonstrate that by using the proposed ceramic synthesis route it is indeed possible to fabricate LiCoO₂–LLZO composites that deliver a discharge capacity of 118 mA h g⁻¹, which is near the theoretical capacity of LiCoO₂ (115 mA h g⁻¹, 3–4.05 V), with an exceptionally low interfacial resistance of 62 $\Omega \text{ cm}^2$.

Perspectives on cathode composite design for garnet-based SSBs

For the successful design of cathode composites in SSBs, a delicate balance must be maintained between the phase stability of all the cathode constituents and an optimal microstructure (here, LLZO *vs.* LiFePO₄ or LiCoO₂ phases) to ensure sufficient electronic and ionic transport, a sufficiently large active reaction area, and a high cathode loading. These properties are largely determined by the specific ceramic processing route selected as well as the thermal processing range. We demonstrate here that when taking all of these factors into account, LiCoO₂ provides more opportunities for the successful preparation of cathode composites with LLZO than LiFePO₄ owing to the improved interfacial stability of the tandem material if precautions are taken to use a ceramic processing route from the direct transfer of a metal salt to an oxide remaining in the low temperature processing regime. The LiCoO₂–LLZO composite cathodes in the current work, prepared by precursor infiltration into a porous LLZO scaffold using direct metal salt-to-oxide cathode crystallization, clearly offer an improved capacity, degradation rate, and interfacial resistance compared with those of ceramic composite cathodes prepared *via* classic solid-state mixing from crystalline powders with alteration of the sintering protocol using a Li–B–O sintering agent (Fig. 1a and 5 and Table 1).^{19,32,33,36,37,51} To the best of our knowledge, the interfacial resistance of the present LiCoO₂–LLZO composite cathodes is the lowest among reported all-oxide Li-garnet SSBs.

From a ceramic manufacturing viewpoint, it is significant to stress that our cathode composite design was achieved without the need for any sintering additives. This translates into more “active” volume being available for filling cathode materials, thereby opening further engineering opportunities for optimization by material processing design. Ideally, an increase of the cathode loading and decrease of porous LLZO are required toward practical application (*e.g.* areal cathode loading $\sim 3 \text{ mA h cm}^{-2}$ for a $\sim 120 \mu\text{m}$ -thick cathode composite^{77,78}). The areal cathode loading in the tested LCO–LLZO cathode composite (Fig. 4f) was 0.73 mg cm⁻² (0.084 mA h cm⁻²) (Table 1), which is below the level required for practical application. In recent studies in which a similar concept of an infiltrated all-oxide cathode in all-solid-state sodium batteries (ASSNBs) was implemented, a high cathode loading up to 6.2 mg cm⁻² (0.6 mA h cm⁻²) was achieved.^{79,80} However, this approach required several repeated steps of infiltration and heat treatment and an ultra-thick $\sim 1 \text{ mm}$ -thick porous ionic scaffold, thus still limiting practical application. The fabrication of a highly porous ionic scaffold that can afford more than 90 wt% or 80 vol% of active materials using freeze-tape-casting or inverse-opal-type template methods appears to be a promising option.^{27,81,82} In all of the methods, the use of a dispersant would increase the uniformity and ordering of the pore distribution further and may be considered for future improvement. A more practical strategy toward a cathode with high LiCoO₂ loading would be to reconstruct the current cathode composite preparation by simply reversing the preparation order between LiCoO₂ and LLZO





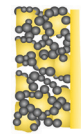


Fig. 5 Comparison of the total interfacial resistance vs. processing temperature of all-oxide Li-garnet SSBs based on layered cathode composites. Three different types of all-oxide cathodes are categorized with respect to the processing strategies: (i) all-oxide cathode w/additives,^{19,32,36} (ii) all-oxide cathode without porous LLZO,³⁷ and (iii) all-oxide cathode with porous LLZO.⁵¹ The numbers indicate the specific capacity (mA h g^{-1}). The conditions for processing and testing are based on Table 1. This study presents the lowest interfacial resistance with the desired specific capacity among reported all-oxide Li-garnet SSBs.

(Fig. S14, ESI[†]), with LiCoO_2 as the sintered porous scaffold and direct synthesis of the LLZO network onto the porous surface of LiCoO_2 . Regarding the rate performance, operating at room temperature under higher current ($>0.05\text{C}$) is desired. We propose that the rate-limiting step in a full cell ($\text{LiCoO}_2\text{-LLZO|LLZO|Li}$) is either charge transport or electronic conduction at the LCO/LLZO interface, which is from the polarization process, $(RQ)^4$, at mid frequencies ($\sim 320\text{ Hz}$) (Fig. 4g). Nonetheless, purely by adapting the ceramic synthesis approach to move radically away from previous attempts using crystalline powder constituents of the cathode *via* casting or other routes but with the direct formation of the active cathode from metal salt to oxide *via* a precursor solution and infiltration within the porous LLZO scaffold, good bonding and low interfacial resistance between the active materials and LLZO electrolyte were achieved at the relatively low processing temperature of $700\text{ }^\circ\text{C}$.

In summary, using crystalline powders of LLZO and LiCoO_2 , good mechanical bonding is hardly achieved at $700\text{ }^\circ\text{C}$,³⁵ and high interfacial resistance is inevitable if the temperature is higher than that required for good solid-solid mechanical bonding (*i.e.*, $>1000\text{ }^\circ\text{C}$) because of possible side reactions.³⁷ With additives, there has been a promising report,¹⁹ however, further engineering to achieve reduced additive loading or alternative processing such as additive coatings on cathode particles is required. Regardless of the cathode preparation methods, ultra-fast sintering strategies^{83,84} can further help to achieve chemically sharp but metallurgically strong-enough interfacial bonding for enhanced performance especially for all-oxide cathode composites for SSBs. With society's need for low-cost and mass-manufacturable processing for cathode composites, we conclude that the presented procedure is inexpensive, rapid, and potentially adaptable for large-scale

Table 1 Comparison of the preparation and performance of layered cathode-based all-oxide Li-garnet SSBs reported in the literature

Description	Chemistry and processing			Electrochemical performance							
	Cathode composition	Processing method	Temp. [$^\circ\text{C}$]	Volt. range [V]	C-Rate or current density	Initial interfacial resistance [Ohm cm^2]	First discharge capacity [mA h g^{-1}]	Capacity loss [$\text{mA h g}^{-1}/\text{cycles}$]	Temp. [$^\circ\text{C}$]	Active material loading [mg cm^{-2}]	Ref.
All-oxide cathode with additives 	$\text{LiCoO}_2 + \text{LLZO} + \text{Li}_{2.3}\text{C}_{0.7}\text{B}_{0.3}\text{O}_3$	Solid-state sintering	700	3–4.05	0.05C	270	106	39/40	100	1	19
	$\text{LiCoO}_2 + \text{Li}_3\text{BO}_3 + \text{In}_2\text{SnO}_5$ (ITO)	Solid-state sintering	700	2.8–4.3	0.007C	>2000	69.6	n.a.	80	4	32
	$\text{LiCoO}_2 + \text{LLZO} + \text{Li}_3\text{BO}_3$	Sol-gel mixed w/LBO	700	2.5–4.2	14 mA cm^{-2}	n.a.	0.6–7	2/5	60	n.a.	33
	NMC + ITO + Li_3BO_3 w Li-Ti-O coating	Solid-state sintering	700	3–4.6	5 mA cm^{-2}	7400	112	65.3/5	80	1	36
All-oxide cathode 	$\text{LiCoO}_2 + \text{LLZO}$	Solid-state sintering	1050	2.4–3.6	50 mA cm^{-2}	1138	117	81/100	50	12.6	37
All-oxide cathode with porous LLZO scaffold 	$\text{LiCoO}_2 + \text{porous LLZO scaffold}$	Solution infiltration	600	3–4.2	0.016C	>8000	18	6/10	80	2.9	51
	$\text{LiCoO}_2 + \text{porous LLZO scaffold}$	Solution infiltration	700	3–4.05	0.05C	62	118	3/14	80	0.73	This study



implementation, as it is widely used in the fields of supported catalysts and solid-oxide fuel cells.⁸⁵

Conclusion

The performance of all-oxide SSBs is often limited by the poor cathode–electrolyte contact and high interfacial impedance arising during fabrication. There are limited reports available on the realization of Li-garnet-based SSBs without the use of a high-temperature process (> 1000 °C), sintering additives, or a fluid electrolyte (polymer-gel, liquid electrolyte), which leads to concerns about the interfacial stability, cathode loading, and safety. In this work, we proposed an alternative ceramic processing strategy to assemble an oxide-based cathode composite based on the most common cathodes of LiFePO₄ and LiCoO₂ (Fig. 6). Thermal heating of the LiFePO₄–Li₇La₃Zr₂O₁₂ (LLZO) interface over 300 °C leads to interfacial decomposition and phase changes due to the poor thermal stability. As a result, the Li-garnet SSB starting with the LiFePO₄ cathode exhibited a reduction of the voltage plateau from 3.2 V (LiFePO₄) to 2.5 V (Li₃Fe₂(PO₄)₃). With such a limited thermal processing window, we propose that the use of a hybrid cathode is currently a feasible option but recommend all-oxide processing with a suitable cathode coating⁴⁷ and cathode firing in a low oxygen partial pressure (e.g., H₂/Ar gas).⁴¹ Taking key processing factors such as interfacial stability vs. temperature into account, we see that LiCoO₂ provides more opportunities for successful preparation and a wider degree of freedom in the processing window of cathode composites with LLZO than LiFePO₄. In particular, the presented LiCoO₂–LLZO composite cathodes prepared through

direct synthesis from metal salts to the oxide cathode in a porous LLZO scaffold clearly demonstrate processing capability that allows good mechanical contact without adverse interfacial reactions at the unusually low processing temperature of 700 °C. Importantly, the additive-free (resp. sinter-agent free) cathode composite results in the lowest interfacial resistance among reported all-oxide Li-garnet SSBs. We can widely adapt this methodology to the exploration of other cathode materials or electrolyte preparation for cathode composites. For example, altered strategies toward higher cathode loading may be the direct synthesis of a Li-ion conductor (e.g., LLZO) in a sintered porous LiCoO₂ scaffold (Fig. S7, ESI†). In addition, we foresee that the processing temperature of the method we present here can potentially be reduced further by controlling the crystallization temperature in the metal salts to oxide transfer of the cathode phase through careful selection of metal salts and their melting points, and employment of organics with altered chain length (Fig. 6). With the help of crystallization kinetics information, gained by constructing time–temperature–transformation (TTT)⁸⁶ diagrams using differential scanning calorimetry, we believe that novel cathode processing guidelines can be further developed.

Experimental details

Li-garnet electrolyte and porous Li-garnet scaffold

Solid-state synthesis. The solid electrolyte, Li_{6.5}La₃Zr_{1.5}Ta_{0.5}O₁₂ (LLZO:Ta), was prepared by solid-state synthesis. A stoichiometric amount of La(OH)₃ (Sigma-Aldrich, 99.9%), ZrO₂ (Sigma-Aldrich, 99.9%), and Ta₂O₅ (Sigma-Aldrich, 99.99%),

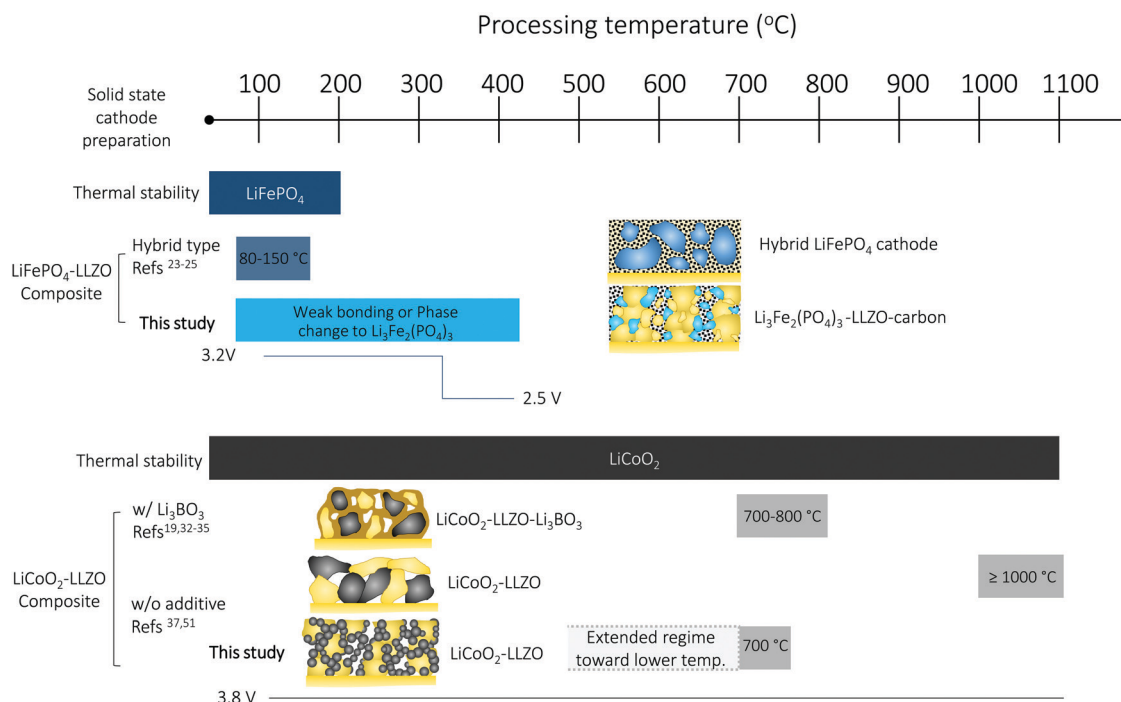


Fig. 6 Overview of the cathode composite design and ceramic processing choices of all-oxide Li-garnet SSBs based on LiFePO₄- and LiCoO₂-based cathode composites: processing temperature vs. chemical and mechanical stability.



Conflicts of interest

The authors declare no conflicts of interest.

Acknowledgements

This publication is based on work funded by the Skolkovo Institute of Science and Technology (Skoltech) through the MIT Skoltech program under contract number 6937431. Structural characterization of the materials was conducted under the MRSEC Program of the National Science Foundation under award DMR-1419807. J. L. M. R. thanks the Thomas Lord Foundation for financial support. We thank Prof. Michal Struzik and Dr. Juan Carlos Gonzalez-Rosillo for the initial help on solid electrolyte synthesis and current collector preparation.

References

- J. Janek and W. G. Zeier, *Nat. Energy*, 2016, **1**, 1–4.
- K. Kerman, A. Luntz, V. Viswanathan, Y.-M. Chiang and Z. Chen, *J. Electrochem. Soc.*, 2017, **164**, A1731–A1744.
- A. J. Samson, K. Hofstetter, S. Bag and V. Thangadurai, *Environ. Sci.*, 2019, **12**, 2957–2975.
- R. Pfenninger, M. Struzik, I. Garbayo, E. Stimp and J. L. M. Rupp, *Nat. Energy*, 2019, **4**, 475–483.
- C. Tsai, V. Roddatis, C. V. Chandran, Q. Ma, S. Uhlenbruck, M. Bram, P. Heitjans and O. Guillon, *ACS Appl. Mater. Interfaces*, 2016, **8**, 10617–10626.
- A. Sharafi, E. Kazyak, A. L. Davis, S. Yu, T. Thompson, D. J. Siegel, N. P. Dasgupta and J. Sakamoto, *Chem. Mater.*, 2017, **29**, 7961–7968.
- B. J. Neudecker, N. J. Dudney and J. B. Bates, *J. Electrochem. Soc.*, 2000, **147**, 517.
- J. B. Bates, N. J. Dudney, B. Neudecker, A. Ueda and C. D. Evans, *Solid State Ionics*, 2000, **135**, 33–45.
- J. Li, C. Ma, M. Chi, C. Liang and N. J. Dudney, *Adv. Energy Mater.*, 2015, **5**, 1–6.
- Y. Zhu, M. Gonzalez-Rosillo, J. C. Balaish, Z. D. Hood, K. J. Kim and J. L. M. Rupp, *Nat. Rev. Mater.*, 2020, in Press.
- G. T. Hitz, D. W. McOwen, L. Zhang, Z. Ma, Z. Fu, Y. Wen, Y. Gong, J. Dai, T. R. Hamann, L. Hu and E. D. Wachsman, *Mater. Today*, 2019, **22**, 50–57.
- X. Han, Y. Gong, K. Fu, X. He, G. T. Hitz, J. Dai, A. Pearse, B. Liu, H. Wang, G. Rubloff, Y. Mo, V. Thangadurai, E. D. Wachsman and L. Hu, *Nat. Mater.*, 2017, **16**, 572–579.
- N. J. Taylor, S. Stangeland-Molo, C. G. Haslam, A. Sharafi, T. Thompson, M. Wang, R. Garcia-Mendez and J. Sakamoto, *J. Power Sources*, 2018, **396**, 314–318.
- F. Flatscher, M. Philipp, S. Ganschow, H. M. R. Wilkening and D. Rettenwander, *J. Mater. Chem. A*, 2020, **8**, 15782–15788, DOI: 10.1039/c9ta14177d.
- T. Deng, X. Ji, Y. Zhao, L. Cao, S. Li, S. Hwang, C. Luo, P. Wang, H. Jia, X. Fan, X. Lu, D. Su, X. Sun, C. Wang and J. Zhang, *Adv. Mater.*, 2020, **2000030**, 2000030.
- J. Duan, L. Huang, T. Wang, Y. Huang, H. Fu, W. Wu, W. Luo and Y. Huang, *Adv. Funct. Mater.*, 2020, **30**, 1–7.
- C. Wang, K. Fu, S. P. Kammampata, D. W. McOwen, A. J. Samson, L. Zhang, G. T. Hitz, A. M. Nolan, E. D. Wachsman, Y. Mo, V. Thangadurai and L. Hu, *Chem. Rev.*, 2020, **10**, 4257–4300.
- F. Hao, F. Han, Y. Liang, C. Wang and Y. Yao, *MRS Bull.*, 2018, **43**, 746–751.
- F. Han, J. Yue, C. Chen, N. Zhao, X. Fan, Z. Ma, T. Gao, F. Wang, X. Guo and C. Wang, *Joule*, 2018, **2**, 497–508.
- S. Randau, D. A. Weber, O. Kötz, R. Koerver, P. Braun, A. Weber, E. Ivers-Tiffée, T. Adermann, J. Kulisch, W. G. Zeier, F. H. Richter and J. Janek, *Nat. Energy*, 2020, **5**, 1–12.
- Y. Kato, S. Hori, T. Saito, K. Suzuki, M. Hirayama, A. Mitsui, M. Yonemura, H. Iba and R. Kanno, *Nat. Energy*, 2016, **1**, 16030.
- Z. Bi, N. Zhao, L. Ma, Z. Fu, F. Xu, C. Wang and X. Guo, *Chem. Eng. J.*, 2020, **387**, 124089.
- F. Du, N. Zhao, Y. Li, C. Chen, Z. Liu and X. Guo, *J. Power Sources*, 2015, **300**, 24–28.
- Y. Li, B. Xu, H. Xu, H. Duan, X. Lü, S. Xin, W. Zhou, L. Xue, G. Fu, A. Manthiram and J. B. Goodenough, *Angew. Chem., Int. Ed.*, 2017, **56**, 753–756.
- W. Luo, Y. Gong, Y. Zhu, Y. Li, Y. Yao, Y. Zhang, K. K. Fu, G. Pastel, C. F. Lin, Y. Mo, E. D. Wachsman and L. Hu, *Adv. Mater.*, 2017, **29**, 1606042, DOI: 10.1002/adma.201606042.
- Y. Shao, H. Wang, Z. Gong, D. Wang, B. Zheng, J. Zhu, Y. Lu, Y. S. Hu, X. Guo, H. Li, X. Huang, Y. Yang, C. W. Nan and L. Chen, *ACS Energy Lett.*, 2018, **3**, 1212–1218.
- E. Yi, H. Shen, S. Heywood, J. Alvarado, D. Y. Parkinson, G. Chen, S. W. Sofie, M. M. Doeff, S. W. So and M. M. Doe, *ACS Appl. Energy Mater.*, 2020, **3**, 170–175.
- Y. Lu, X. Huang, Z. Song, K. Rui, Q. Wang, S. Gu, J. Yang, T. Xiu, M. E. Badding and Z. Wen, *Energy Storage Mater.*, 2018, **15**, 282–290, DOI: 10.1016/j.ensm.2018.05.018.
- J. Liu, X. Gao, G. O. Hartley, G. J. Rees, C. Gong, F. H. Richter, J. Janek, Y. Xia, A. W. Robertson, L. R. Johnson and P. G. Bruce, *Joule*, 2020, **4**, 101–108.
- M. Naguib, A. Sharafi, E. C. Self, H. M. Meyer, J. Sakamoto and J. Nanda, *ACS Appl. Mater. Interfaces*, 2019, **11**, 42042–42048, DOI: 10.1021/acsami.9b11439.
- K. Liu, Y. Liu, D. Lin, A. Pei and Y. Cui, *Sci. Adv.*, 2018, **4**, eaas9820, DOI: 10.1126/sciadv.aas9820.
- T. Liu, Y. Ren, Y. Shen, S.-X. X. Zhao, Y. Lin and C.-W. W. Nan, *J. Power Sources*, 2016, **324**, 349–357.
- M. Shoji, H. Munakata and K. Kanamura, *Front. Energy Res.*, 2016, **4**, 1–7.
- S. Ohta, J. Seki, Y. Yagi, Y. Kihira, T. Tani and T. Asaoka, *J. Power Sources*, 2014, **265**, 40–44.
- K. Park, B. C. Yu, J. W. Jung, Y. Li, W. Zhou, H. Gao, S. Son and J. B. Goodenough, *Chem. Mater.*, 2016, **28**, 8051–8059.
- L. Ting, Z. Yibo, Z. Xue, W. Lei, Z. Shi-Xi, L. Yuan-Hua, S. Yang, L. Jun, L. Liangliang, N. Ce-Wen, T. Liu, Y. Zhang,



- X. Zhang, L. Wang, S. X. Zhao, Y. H. Lin, Y. Shen, J. Luo, L. Li and C. W. Nan, *J. Mater. Chem. A*, 2018, **6**, 4649–4657.
- 37 C. L. Tsai, Q. Ma, C. Dellen, S. Lobe, F. Vondahlen, A. Windmüller, D. Grüner, H. Zheng, S. Uhlenbruck, M. Finsterbusch, F. Tietz, D. Fattakhova-Rohlfing, H. P. Buchkremer and O. Guillon, *Sustainable Energy Fuels*, 2019, **3**, 280–291.
- 38 Y. Xiao, Y. Wang, S. H. Bo, J. C. Kim, L. J. Miara and G. Ceder, *Nat. Rev. Mater.*, 2019, **5**, 105–126.
- 39 L. Miara, A. Windmüller, C. L. Tsai, W. D. Richards, Q. Ma, S. Uhlenbruck, O. Guillon and G. Ceder, *ACS Appl. Mater. Interfaces*, 2016, **8**, 26842–26850.
- 40 J. Wakasugi, H. Munakata and K. Kanamura, *Electrochemistry*, 2017, **85**, 77–81.
- 41 Y. Ren, T. Liu, Y. Shen, Y. Lin and C. W. Nan, *J. Mater.*, 2016, **2**, 256–264.
- 42 S. Ohta, S. Komagata, J. Seki, T. Saeki, S. Morishita and T. Asaoka, *J. Power Sources*, 2013, **238**, 53–56.
- 43 N. C. Rosero-Navarro and K. Tadanaga, *Sintering Additives for Garnet-Type Electrolytes*, Springer, 2000.
- 44 W. D. Kingery and M. D. Narasimhan, *J. Appl. Phys.*, 1959, **30**, 307–310.
- 45 R. A. Jonson and P. J. McGinn, *Solid State Ionics*, 2018, **323**, 49–55.
- 46 R. H. Shin, S. I. Son, Y. S. Han, Y. Do Kim, H. T. Kim, S. S. Ryu and W. Pan, *Solid State Ionics*, 2017, **301**, 10–14.
- 47 Y. Xiao, L. J. Miara, Y. Wang and G. Ceder, *Joule*, 2019, **3**, 1252–1275.
- 48 S. Xu, D. W. McOwen, C. Wang, L. Zhang, W. Luo, C. Chen, Y. Li, Y. Gong, J. Dai, Y. Kuang, C. Yang, T. R. Hamann, E. D. Wachsman and L. Hu, *Nano Lett.*, 2018, **18**, 3926–3933.
- 49 J. van den Broek, S. Afyon and J. L. M. Rupp, *Adv. Energy Mater.*, 2016, **6**, 1–11.
- 50 K. Fu, Y. Gong, G. T. Hitz, D. W. McOwen, Y. Li, S. Xu, Y. Wen, L. Zhang, C. Wang, G. Pastel, J. Dai, B. Liu, H. Xie, Y. Yao, E. D. Wachsman and L. Hu, *Energy Environ. Sci.*, 2017, **10**, 1568–1575.
- 51 Y. Ren, T. Liu, Y. Shen, Y. Lin and C. W. Nan, *Ionics*, 2017, **23**, 2521–2527.
- 52 R. Murugan, V. Thangadurai and W. Weppner, *Angew. Chem., Int. Ed.*, 2007, **46**, 7778–7781.
- 53 D. Rettenwander, G. Redhammer, F. Preishuber-Pflügl, L. Cheng, L. Miara, R. Wagner, A. Welzl, E. Suard, M. M. Doeff, M. Wilkening, J. Fleig and G. Amthauer, *Chem. Mater.*, 2016, **28**, 2384–2392.
- 54 N. Nitta, F. Wu, J. T. Lee and G. Yushin, *Mater. Today*, 2015, **18**, 252–264.
- 55 B. Lung-Hao, Hu, F. Y. Wu, C. Te Lin, A. N. Khlobystov and L. J. Li, *Nat. Commun.*, 2013, **4**, 1–7.
- 56 C. Wang and J. Hong, *Electrochem. Solid-State Lett.*, 2007, **10**, A65.
- 57 S. Y. Chung, J. T. Bloking and Y. M. Chiang, *Nat. Mater.*, 2002, **1**, 123–128.
- 58 J. Ni and Y. Wang, *RSC Adv.*, 2015, **5**, 30537–30541.
- 59 C. Masquelier, A. K. Padhi, K. S. Nanjundaswamy and B. Goodenough, *J. Solid State Chem.*, 1998, **135**, 228–234.
- 60 L. J. Miara, W. D. Richards, Y. E. Wang and G. Ceder, *Chem. Mater.*, 2015, **27**, 4040–4047.
- 61 G. Vardar, W. J. Bowman, Q. Lu, J. Wang, R. J. Chater, A. Aguadero, R. Seibert, J. Terry, A. Hunt, I. Waluyo, D. D. Fong, A. Jarry, E. J. Crumlin, S. L. Hellstrom, Y. M. Chiang and B. Yildiz, *Chem. Mater.*, 2018, **30**, 6259–6276.
- 62 Y. Ren, T. Liu, Y. Shen, Y. Lin and C. Nan, *J. Mater.*, 2016, **2**, 256–264.
- 63 G. Larraz, A. Orera and M. L. Sanjuán, *J. Mater. Chem. A*, 2013, **1**, 11419–11428.
- 64 F. Tietz, T. Wegener, M. T. Gerhards, M. Giarola and G. Mariotto, *Solid State Ionics*, 2013, **230**, 77–82.
- 65 T. Gross and C. Hess, *J. Power Sources*, 2014, **256**, 220–225.
- 66 M. D. Levi, *J. Electrochem. Soc.*, 1999, **146**, 1279.
- 67 W. Zhang, F. H. Richter, S. P. Culver, T. Leichtweiss, J. G. Lozano, C. Dietrich, P. G. Bruce, W. G. Zeier and J. Janek, *ACS Appl. Mater. Interfaces*, 2018, **10**, 22226–22236.
- 68 R. Koerver, I. Aygün, T. Leichtweiß, C. Dietrich, W. Zhang, J. O. Binder, P. Hartmann, W. G. Zeier and J. Janek, *Chem. Mater.*, 2017, **29**, 5574–5582.
- 69 T. Yoshinari, R. Koerver, P. Hofmann, Y. Uchimoto, W. G. Zeier and J. Janek, *ACS Appl. Mater. Interfaces*, 2019, **11**, 23244–23253.
- 70 I. A. J. Gordon, S. Grugeon, H. Takenouti, B. Tribollet, M. Armand, C. Davoisne, A. Débart and S. Laruelle, *Electrochim. Acta*, 2017, **223**, 63–73.
- 71 J. Illig, M. Ender, T. Chrobak, J. P. Schmidt, D. Klotz and E. Ivers-Tiffée, *J. Electrochem. Soc.*, 2012, **159**, A952–A960.
- 72 Y. J. Nam, K. H. Park, D. Y. Oh, W. H. An and Y. S. Jung, *J. Mater. Chem. A*, 2018, **6**, 14867–14875.
- 73 S. P. Culver, R. Koerver, W. G. Zeier and J. Janek, *Adv. Energy Mater.*, 2019, **9**, 1–14.
- 74 Y. Zhu, X. He and Y. Mo, *J. Mater. Chem. A*, 2016, **4**, 3253–3266.
- 75 J. Lu, T. Wu and K. Amine, *Nat. Energy*, 2017, **2**, 17011.
- 76 D. H. S. S. Tan, A. Banerjee, Z. Chen and Y. S. Meng, *Nat. Nanotechnol.*, 2020, **15**, 1–11.
- 77 Y. G. Lee, S. Fujiki, C. Jung, N. Suzuki, N. Yashiro, R. Omoda, D. S. Ko, T. Shiratsuchi, T. Sugimoto, S. Ryu, J. H. Ku, T. Watanabe, Y. Park, Y. Aihara, D. Im and I. T. Han, *Nat. Energy*, 2020, **5**, 299–308, DOI: 10.1038/s41560-020-0575-z.
- 78 P. Albertus, S. Babinec, S. Litzelman and A. Newman, *Nat. Energy*, 2018, **3**, 16–21.
- 79 C. L. Tsai, T. Lan, C. Dellen, Y. Ling, Q. Ma, D. Fattakhova-Rohlfing, O. Guillon and F. Tietz, *J. Power Sources*, 2020, **476**, 228666.
- 80 T. Lan, C.-L. Tsai, F. Tietz, X.-K. Wei, M. Heggen, R. E. Dunin-Borkowski, R. Wang, Y. Xiao, Q. Ma and O. Guillon, *Nano Energy*, 2019, **65**, 104040.
- 81 J. S. Sakamoto and B. Dunn, *J. Mater. Chem.*, 2002, **12**, 2859–2861.
- 82 M. Hara, H. Nakano, K. Dokko, S. Okuda, A. Kaeriyama and K. Kanamura, *J. Power Sources*, 2009, **189**, 485–489.



- 83 G. Zhong, C. Wang, R. Wang, W. Ping, S. Xu, H. Qiao, M. Cui, X. Wang, Y. Zhou, D. J. Kline, M. R. Zachariah and L. Hu, *Energy Storage Mater.*, 2020, **30**, 385–391.
- 84 C. Wang, W. Ping, Q. Bai, H. Cui, R. Hensleigh, R. Wang, A. H. Brozena, Z. Xu, J. Dai, Y. Pei, C. Zheng, G. Pastel, J. Gao, X. Wang, H. Wang, J.-C. Zhao, B. Yang, X. (Rayne) Zheng, J. Luo, Y. Mo, B. Dunn and L. Hu, *Science*, 2020, **368**, 521–526.
- 85 J. T. S. Irvine, D. Neagu, M. C. Verbraeken, C. Chatzichristodoulou, C. Graves and M. B. Mogensen, *Nat. Energy*, 2016, **1**, 1–13.
- 86 J. L. M. Rupp, B. Scherrer, N. Schäuble and L. J. Gauckler, *Adv. Funct. Mater.*, 2010, **20**, 2807–2814.
- 87 C. A. Schneider, W. S. Rasband and K. W. Eliceiri, *Nat. Methods*, 2012, **9**, 671–675.

